Experimental observation of the electron beam focusing effect induced by plasma currents with opposite directions

Jie-Jie Lan,[1] Zhang-Hu Hu,[1,*] Zhao-Hui Ran,[2] Jia Li,[2] You-Wei Zhou,[2] Shu-Chun Cao,[2,3] Rui Cheng,[2] Yan-Hong Chen,[2] Wen-Bing Yan,[2] Quan-Tang Zhao,[2,3,†] Yong-Tao Zhao,[4] Zi-Min Zhang,[2,3] and You-Nian Wang[1]

[1]*School of Physics, Dalian University of Technology, Dalian 116024, People's Republic of China*

[2]*Institute of Modern Physics, Chinese Academy of Sciences, Lanzhou 730000, People's Republic of China*

[3]*School of Nuclear Science and Technology, University of Chinese Academy of Sciences, Beijing 100049, People's Republic of China*

[4]*School of Physics, Xi'an Jiaotong University, Xi'an 710049, People's Republic of China*

(Received 9 June 2023; revised 24 September 2023; accepted 13 November 2023; published 4 December 2023)

We report on the experimental observation of the focusing effect of a 50 MeV accelerator electron beam in a gas-discharge plasma target. The plasma is generated by igniting an electric discharge in two collinear quartz tubes, with the currents up to 1.5 kA flowing in opposite directions in either of the two tubes. In such plasma current configuration, the electron beam is defocused in the first discharge tube and focused with a stronger force in the second one. With symmetric plasma currents, asymmetric effects are, however, induced on the beam transport process and the beam radius is reduced by a factor of 2.6 compared to the case of plasma discharge off. Experimental results are supported by two-dimensional particle-in-cell simulations.

DOI: 10.1103/PhysRevE.108.065203

I. INTRODUCTION

High-quality electron beams are nowadays widely used for many applications such as, for instance, the radiation ranges from coherent terahertz [1–3] to gamma rays [4–6], the e^+e^- high-energy linear colliders [7], and plasma-based accelerators [8]. For all these applications, electron beams with high peak current, low energy spread, and small beam emittance and size are critical. At present, electron beams can be produced from conventional RF accelerators or laser-plasma interactions. Although the laser wakefield accelerators can accelerate an electron beam to multi-GeV in cm-scale structures, the produced beam usually has a large angular divergence of several mrad [9]. On the other hand, the beam from the conventional RF accelerators are controllable and are of good quality with low emittance and energy spread, but usually has a large size and duration. Thus, a proper focusing system is needed for both types of electron beams before practical applications.

One option would be using conventional focusing systems, such as solenoids [10,11] and quadrupole magnets [12,13]. However, solenoid magnets are only suitable for focusing electron beams in low-energy sections (i.e., a few MeV or less). In addition, a quadrupole defocuses the electron beam in the plane orthogonal to the focusing plane and must be used in groups that cannot meet the requirements of miniaturization. Plasma-based lenses promise to pave the way for radially symmetric focusing and kT/m-level focusing gradients to overcome the drawbacks of conventional focusing schemes.

In plasma lenses, electron beams can be focused (i) by the azimuthal magnetic field induced by the plasma discharge current (active plasma lenses, APLs) [12,14–17], and (ii) by the self-generated magnetic field due to unneutralized beam current in plasmas (passive plasma lenses, PPLs) [18–20]. Discharge-capillary APLs have been used in laser-plasma accelerators [12] and conventional RF accelerators [16] with a focusing gradient in excess of 3 kT/m [21]. The uniformity of the discharge current is particularly important for an APL, which has been measured in experiments [14,21]. Great efforts are currently ongoing in several groups to increase the radial uniformity and thus preserve the emittance of the beam such as, for instance, by changing from a light gas species to a heavier gas species [15], increasing the plasma temperature, and discharge current [14]. The PPL offers a gentler focus compared to the APL, still of interest to be used in accelerators. A laser-ionized, beam-driven, underdense, passive thin plasma lens with tunable, compact, and little spherical aberrations has been designed at the SLAC National Accelerator Laboratory's FACET-II facility [19]. The electron beam can reach a final beta function that is half that achievable by the FACET-II magnetic final focus system. In addition, Thaury *et al*. [22] have demonstrated the collimation of an electron beam by a laser-plasma lens, and the beam divergence was reduced by a factor of two for the whole beam and a factor of 2.6 for its high-energy part.

Recently, plasma lenses have been adopted in the generation of gamma-ray beams [4,6] with small divergence and spot size, which is essential for high-resolution radiography. In our previous work [4], we also proposed a scheme with validated simulations to show the potential of a plasma lens in high-quality gamma-ray generation, in which an accelerator electron beam is focused with a plasma lens before passing through a conversion target. It is shown that the spot size and divergence of the emitted photons in the case with a plasma lens are reduced significantly compared to the case without the plasma lens. In this work, as a first step toward

*zhanghu@dlut.edu.cn

†zhaoquantang@impcas.ac.cn

the experimental validation of the proposed scheme, a plasma lens experiment was carried out at the Institute of Modern Physics (IMP), Chinese Academy of Sciences by employing a gas-discharge plasma target [23] and accelerator electron beams. The plasma is generated by igniting an electric discharge in two 7.8-cm-long collinear quartz tubes, with the currents up to ∼1.5 kA flowing in opposite directions in either of the two tubes. In such a plasma current configuration, the electron beam is defocused in the first tube and focused in the second one. With symmetric plasma currents, asymmetric effects on the beam transport process are found and the beam radius is reduced by a factor of 2.6 compared to the case of discharge off. Experimental results are supported by two-dimensional (2D) particle-in-cell (PIC) simulations. This paper is organized as follows. The experimental setup is described in Sec. II, and experimental results are presented in Sec. III. In Sec. IV, we discuss the asymmetric effects induced by plasma currents and describe the simulation results. And finally, we summarize the work in Sec. V.

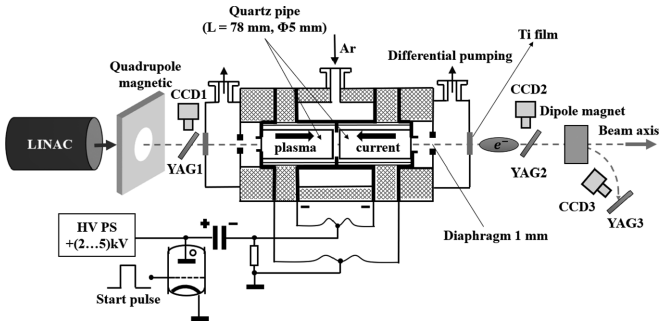

FIG. 1. Schematic of the experimental setup. An accelerator electron beam propagates through a high-voltage direct current discharge plasma target to either a transverse beam size diagnostic (yttrium aluminium garnet) or energy distribution diagnostic (dipole magnetic). In order to maintain the accelerator vacuum, two 10 μm titanium films are used to separate the plasma chamber from the upstream accelerating tube. The electron beam passing through the target is comoving with the discharge current in the first quartz tube and then countermoving in the second one.

II. EXPERIMENTAL SETUP

A. The experimental platform

The electron linear accelerator for the experimental platform, which was designed and developed at IMP for high energy electron radiography [24,25], consists of two different types of electron guns: a thermionic cathode RF gun and a photocathode RF gun (under construction). The macropulse bunch at the exit of the 1.5-cell S-band thermionic cathode gun with 70 MV/m acceleration field strength has a large energy spread (1 − 4 MeV) and undesirable beam quality. Downstream of the gun are four quadrupole magnets to match the transverse (which is perpendicular to the beam propagation direction) distribution of the macropulse bunch. Further downstream is an alpha magnet [25] to realize the longitudinal compression of the beam and reduce the energy spread in the low-energy beamline. Then the beam enters into a 3 m-long S-band accelerating tube which operates atthe $2\pi/3$ mode and with the maximum acceleration gradient 22.5 MV/m. Subsequently, up to 50 MeV macropulse electron beam with short pulse width (0.7 ps), low energy spread (0.13%), and low emittance (4.43 π mm mrad) is obtained at the exit of the accelerating tube. Finally, the high-energy electron beam enters the plasma target. Details of the gas-discharge plasma device are introduced in Sec. II B. Quadrupole magnets between the accelerating tube and plasma target and the steering coils during the beamline are used to aid in focusing the beam and aligning the beam to the plasma.

B. The gas-discharge plasma device

Figure 1 shows the schematic of the gas-discharge plasma device powered by a type of C1K-3K uninterruptible power system battery of SANTAK. The device has been used for the experimental investigations of ion beam energy loss [23,26] and charge state [27]. The plasma target consists of two 7.8-cm-long collinear quartz tubes with an inner diameter of 5 mm filled with argon gas (1–5 mbar). The plasma is produced during an electric discharge between a central electrode and two grounded electrodes situated at the entrance and exit of the target. A 3 μF capacitor battery charged to 2 − 5 kV initiates a current of up to 1.5 kA in each discharge channel. The maximum plasma electron density n_{pe} produced by the target is about 10^{23} m^{-3} and the temperature inside the quartz tubes is a few eV. It has been designed with one inlet connected with an argon bomb at 1/2 of the total length and two outlets on both sides of the plasma target to maintain a constant backing pressure. In order to maintain the accelerator vacuum, two 10 μm titanium films are used to separate the plasma chamber from the upstream accelerating tube. An off-line optical fiber Mach-Zehnder interferometer at a wavelength of 1.55 μm is used to measure the density of free electrons [28]. The measurement results show the average density of the free electrons along the central axis of the plasma target, and the maximum value of the average plasma density is about 6×10^{22} m^{-3} when the plasma target is in the discharge state of 3 kV-1 mbar. In addition, there are two apertures with 1 mm diameter at the entrance of the first discharge tube and the exit of the second one. This limits the transverse size of the electron beam. The 2D simulations with COMSOL were performed to study the electric discharge process of the plasma target [29], which agrees with the experimental results.

III. EXPERIMENTAL RESULTS

Direct measurements of the beam spot size are performed by the combination of a removable yttrium aluminium garnet (YAG) screen followed by a high-resolution charge coupled device (CCD) camera, as reported in Fig. 1. The imaging system has a resolution of 0.02 mm, which is much smaller than the minimal beam size (i.e., 0.48 mm) observed in the experiment. To account for plasma fluctuations, every measurement is performed from averaging over 50 acquisitions. There are quadrupoles and steering magnets to ensure the beam with a small and symmetric transverse distribution before entering the plasma target. Experimentally, a Rogwski coil is used to infer the discharge current I_{pe}, while a fast current transformer allows the current of the macropulse electron beam

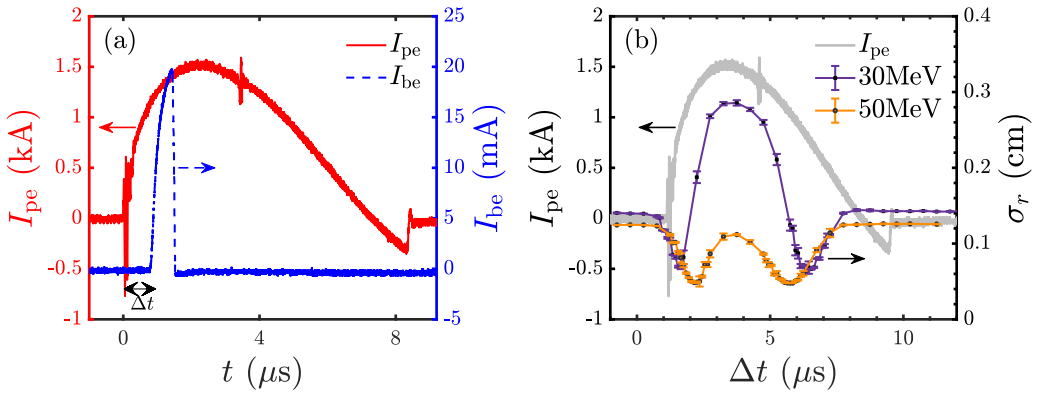

FIG. 2. (a) Current traces of the plasma discharge (red solid line) and electron beam (blue dashed line), and (b) the measured beam spot size (rms) as a function of the delay time between plasma ignition and trigger of the electron beam for two beam energy cases (30 MeV and 50 MeV). The plasma current trace (gray line) is also shown in the figure (b) for illustration. The beam spot size is measured on the first screen (i.e., YAG2-CCD2 shown in Fig. 1) downstream the plasma target, and the distance between the plasma exit and the screen is 22.5 cm.

I_{be}. The current traces of the plasma discharge and electron beam are illustrated in Fig. 2(a). By changing the delay time Δt between plasma ignition and the trigger of the electron beam, the beam can probe the plasma at different discharge stages.

The beam spot size measured on the first screen (i.e., YAG2-CCD2 shown in Fig. 1) downstream the plasma target at different discharge currents is shown in Fig. 2(b) for two beam energy cases (30 MeV and 50 MeV). Note that the spot size (root mean square, rms) σ_r in the figures is obtained by a Gaussian fit of the form $\sim \exp[-\frac{r^2}{2\sigma_r^2}]$. From the discharge current, the plasma lasts about 10 μs. The beam focusing effect can be clearly observed at the rising and falling edges of the plasma current. For a beam energy of 50 MeV, the focusing effect lasts about 3.5 μs, from $\Delta t = 1.2$ μs to 2.7 μs and 4.7 μs to 6.7 μs. The maximum beam focusing (i.e., $\sigma_r = 0.48$ mm) occurs at a delay time $\Delta t = 5.7$ μs after plasma ignition with current $I_{pe} \approx 1$ kA, as shown in Fig. 2(b). Further increase of the plasma current leads to beam overfocusing, as indicated in the figure with peak current $I_{pe} \approx 1.5$ kA. Reducing the beam energy from 50 MeV to 30 MeV, the maximum beam focusing (i.e., $\sigma_r = 0.7$ mm) occurs at a smaller current with $I_{pe} \approx 0.8$ kA, and the overfocusing effect is more significant.

The beam spots measured on the screen are compared for the cases of plasma discharge turned off and on in Figs. 3 (with beam energy 50 MeV) and 4 (with beam energy 30 MeV). The corresponding horizontal (x direction) and vertical (y direction) beam envelope projections in the transverse plane are also shown in the figures. From Fig. 3, the beam spot size σ_r is about 1.25 mm when the discharge is turned off and reduces to 0.48 mm at the maximum focusing, indicating a factor of 2.6 reduction in beam radius. And the density of the electron beam n_{be} is increased by a factor of ~7. The focusing effect can also be observed in Fig. 4 for lower beam energy, in which the beam spot size is reduced by a factor of two when the discharge is turned on with the maximum beam focusing.

IV. DISCUSSION

With the beam and plasma parameters in the experiment, the focusing effect due to beam current can be neglected. The electron beam parameters are as follows: rms radius $\sigma_r = 0.17$ mm limited by the size of the aperture, rms length $\sigma_z = 0.22$ mm measured by the method based on the analysis of the coherent transition radiation energy spectrum [30], and the beam energies ε_{be} measured by a dipole magnet are 50 MeV and 30 MeV. The peak bunch density for the Gaussian-shaped beam is $n_{be} = Q_{be}/\ [e(2\pi)^{3/2}\sigma_r^2\sigma_z] \approx 3 \times 10^{17}\ \mathrm{m}^{-3}$, where $Q_{be} \sim 5$ pC is the total charge of the micropulse electron beam and e is the electronic charge. The self-focusing gradient due to beam current can be computed as [7] $\frac{\partial B_\theta}{\partial r} = 3 \times 10^{-9} n_{be}[\ \mathrm{cm}^{-3}]\mathrm{G/cm} \sim 9\ \mathrm{T/m}$, where B_θ is the azimuthal focusing magnetic field. Assuming the plasma current uniformly distributed in the tube with radius R, one can calculate the magnetic field due to plasma current as a function of the radial positron r using Ampère's law [15]: $B_\theta = \frac{\mu_0 I_{pe} r}{2\pi R^2} = gr$, with g the magnetic field gradient and μ_0 the permeability of vacuum. For the plasma target in the experiment with peak current $I_{pe} \approx 1.5$ kA and $R = 2.5$ mm, we have a magnetic field gradient $g = 48$ T/m, which is much larger than that of the self-focusing gradient. Therefore, the beam self-focusing effect can be neglected, and the focusing phenomenon observed in the experiment should be induced by plasma discharge currents. Note that the wakefield focusing effects, self-driven by the electron beam, can be neglected if $(\sigma_z/\sigma_r)^2 n_{be}/n_{pe} \ll 2(I_{pe}/I_A)(k_{pe}R)^{-2}$ [12], with $k_{pe} = \sqrt{n_{pe}e^2/m_e c^2 \varepsilon_0}$ the plasma wave number, ε_0 the vacuum permittivity, m_e the electron rest mass, c the speed of light, and $I_A \approx 17$ kA the Alfvén current. For the beam and plasma parameters considered here, this condition is well satisfied. Besides, the measured beam spot size soon returns to its initial value after the discharge off, which is the same as that before plasma ignition in Fig. 2(b), indicating negligible influence from plasma wakefields.

The electron beam passing through the plasma target is comoving with the discharge current in the first quartz tube and then countermoving in the second one. In such a plasma current configuration, the electron beam is defocused in the first discharge tube and focused in the second one. The beam focusing effect induced by plasma currents with opposite directions can be understood as follows. Considering the radial

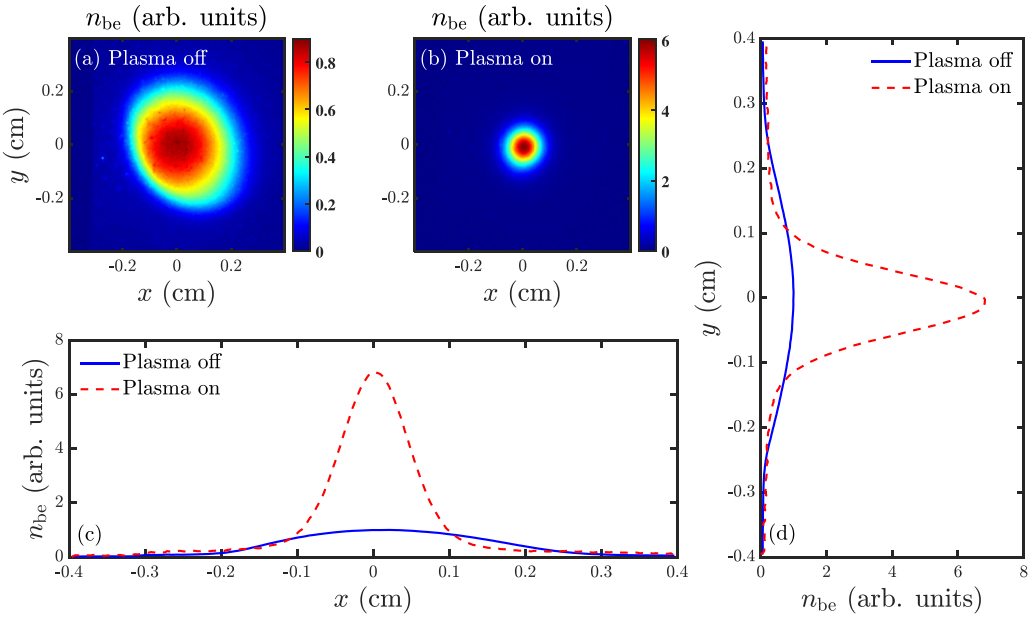

FIG. 3. The beam spot size measured on the first screen downstream the plasma target with the discharge turned off [$\sigma_r = 1.25\,\text{mm}$, (a)] and turned on with a plasma current $I_{pe} \approx 1\,\text{kA}$ [$\sigma_r = 0.48\,\text{mm}$, (b)]. The horizontal (c) and vertical (d) bunch envelopes report the transverse projections of (a) and (b). The beam energy is 50 MeV.

motions of beam electrons in the magnetic fields induced by plasma currents, the evolution of radial momentum satisfies $\mathrm{d}p_r/\mathrm{d}t = ecB_\theta$, with the assumption that the electrons move along the z direction with the velocity $\sim c$. Then the electron radial motion in the first defocusing tube satisfies $\mathrm{d}^2r/\mathrm{d}t^2 = \Gamma^2 r$, where $\Gamma = \sqrt{\frac{ec\mu_0 j_z}{2\gamma_0 m_e}}$, γ_0 is the Lorentz factor of beam electrons, and $j_z = I_{pe}/\pi R^2$ is the plasma current density. Therefore, the radius r of the electron beam increases as a function of the beam travel distance $z = ct$ in the first plasma tube:

$$r_1(z) = A_1 e^{\frac{\Gamma}{c}z} + A_2 e^{-\frac{\Gamma}{c}z} \, (0 \leqslant z \leqslant 7.8\,\text{cm}), \tag{1}$$

as shown in Fig. 5(a) (with the light blue background). The coefficient A_1 and A_2 can be given by $r_1(0) = r_0$ and $r_1'(0) = 0$, where r_0 is the initial radius of the electron beam. With a plasma current $I_{pe} = 1.5\,\text{kA}$ and beam energy $\varepsilon_{be} = 50\,\text{MeV}$, the beam spot size is enlarged by a factor of two at $z_1 = 7.8\,\text{cm}$, the exit of the first tube shown in Fig. 5(a). Then

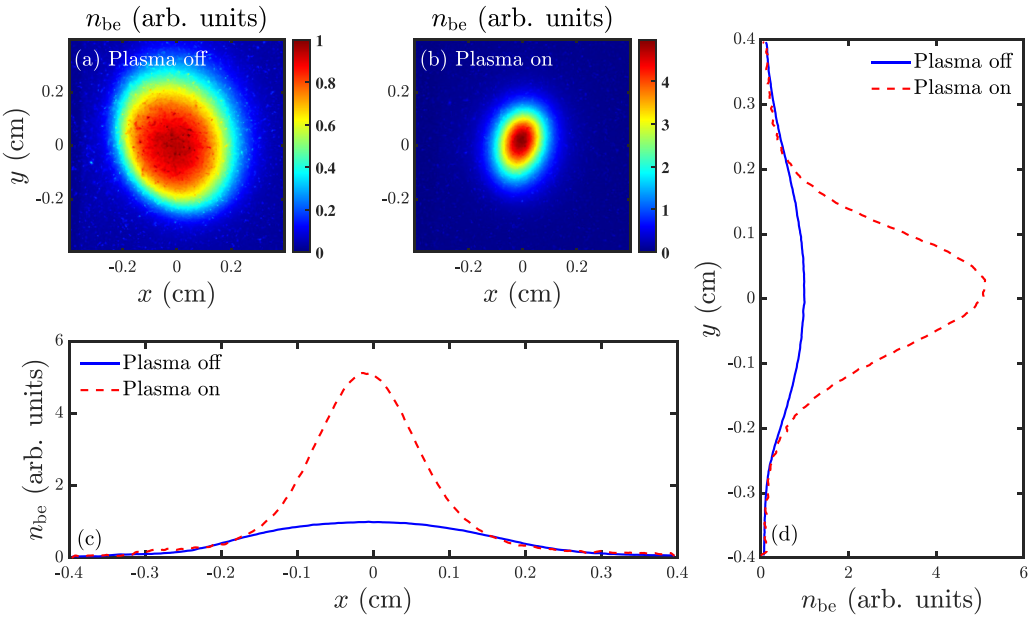

FIG. 4. The beam spot measured on the first screen downstream of the plasma target with the discharge turned off [$\sigma_r = 1.4\,\text{mm}$, (a)] and turned on with a plasma current $I_{pe} \approx 0.8\,\text{kA}$ [$\sigma_r = 0.7\,\text{mm}$, (b)]. The horizontal (c) and vertical (d) bunch envelopes report the transverse projections of (a) and (b). The beam energy is 30 MeV.

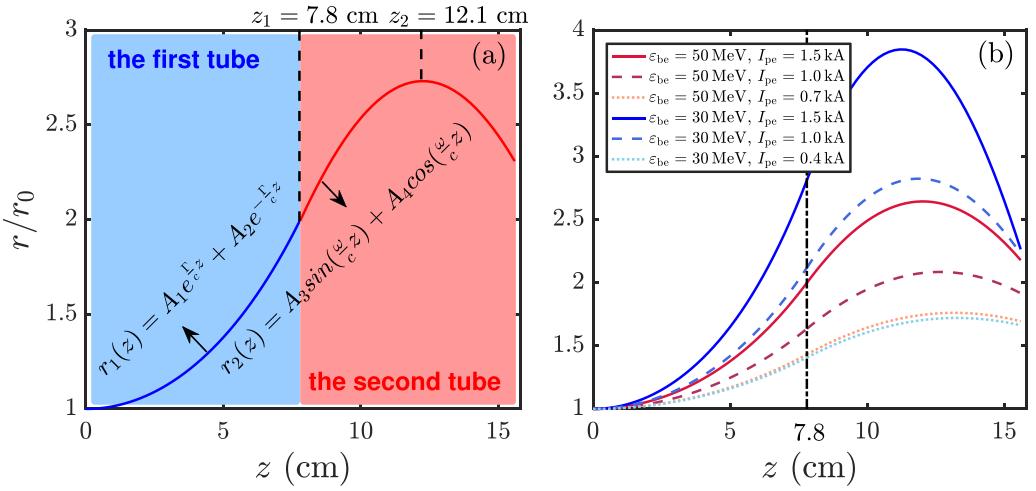

FIG. 5. (a) Evolution of the beam radius r with propagation distance z, where r_0 is the initial radius of the electron beam. Background colors are used to identify the first defocusing tube (light blue) and second focusing tube (light red). (b) The same r/r_0 as (a) with different beam energies [30 MeV and 50 MeV] and discharge currents (from 0 to 1.5 kA).

the beam enters into the second tube with the focusing magnetic field. And the radial motion changes to $d^2r/dt^2 = -\omega^2 r$, where $\omega = \Gamma$ is the betatron frequency. Therefore, the evolution of the beam radius r with the propagation distance z in the second focusing tube is

$$r_2(z) = A_3 \sin\left(\frac{\omega}{c}z\right) + A_4 \cos\left(\frac{\omega}{c}z\right) \ (7.8\,\text{cm} < z \leqslant 15.6\,\text{cm}), \tag{2}$$

as illustrated in Fig. 5(a) (with the light red background), where A_3 and A_4 can be obtained from the conditions of $r_2(z_1) = r_1(z_1)$ and $r_2'(z_1) = r_1'(z_1)$. When the electron beam enters the second quartz tube, the beam size continues to increase until the radial velocity decreases to zero, i.e., $dr_2/dz = 0$ at $z = z_2 = 12.1$ cm. Then the beam electrons move toward beam axis, and the radius decreases gradually. The beam size at the exit of the plasma target is larger than $r_1(0)$, but the beam electrons have a convergence angle, as shown in Fig. 5. The critical point here is that the magnetic field in the plasma tube increases linearly with the radial distance. After being defocused in the first tube, the same beam electron experiences a stronger focusing force (in the second tube) than the defocusing force (in the first tube), and the beam electrons can be focused in the later stage of the second plasma tube (i.e., $12.1\,\text{cm} < z \leqslant 15.6\,\text{cm}$). Finally, we can observe the beam focusing effect in the experiment at the position of the screen, 25.5 cm downstream the plasma target.

To further show the beam focusing effect induced by plasma current, 2D PIC simulations are also performed with the code IBMP [4,31,32]. The code is a 2D3V (two dimensional in space and three dimensional in velocity) relativistic, electromagnetic PIC code. The Maxwell's equations are solved with a finite-difference time-domain (FDTD) method and the numerical integration of the equations of motions for all charged particles is performed by a standard leap-frog algorithm, with the Lorentz forces treated by the Boris rotation. In addition, the periodic, conducting, and perfectly matched layer (PML) absorbing boundary conditions can be adopted in the simulations. The code is parallelized using message passing interface (MPI) through domain decomposition. Also, for the efficiency of parallel computation, a current deposition scheme is designed to conserve charge exactly and there is no need to solve Poisson's equation. The transverse simulation plane is perpendicular to the beam propagation direction (i.e., z axis). The electron beam parameters adopted in the simulations are the same as the experiment. The electron beam passing through the plasma target is first comoving with the discharge current I_{pe} and then countermoving after the central electrode. Between the exit of the plasma target and the imaging system, there is a vacuum drift section of 25.5 cm, which is also considered in the simulation. This way, the magnetic fields experienced by beam electrons can be divided into three regions: (i) a defocusing section ($0 \sim 7.8$ cm), (ii) a focusing section ($7.8 \sim 15.6$ cm), and (iii) a vacuum drift section ($15.6\,\text{cm} \sim$ the end of the beamline). Thus, the transverse magnetic field B_x and B_y can be modeled as

$$\begin{cases} B_x = -g \cdot y \\ B_y = g \cdot x \end{cases}, \quad 0 \leqslant z \leqslant 7.8\,\text{cm}, \qquad \begin{cases} B_x = g \cdot y \\ B_y = -g \cdot x \end{cases}, \quad 7.8\,\text{cm} < z \leqslant 15.6\,\text{cm}, \qquad \begin{cases} B_x = 0 \\ B_y = 0 \end{cases}, \quad 15.6\,\text{cm} < z \leqslant 41.1\,\text{cm}. \tag{3}$$

Figure 6 shows the simulation results of the beam density n_{be} and the transverse phase-space x-p_x distributions with an initial energy of 50 MeV and discharge current $I_{pe} = 1.5$ kA at different beam travel distances. The beam density before entering the plasma in Fig. 6(a) is used for reference, which corresponds to the electron beam with initial radius r_0 at $z = 0$. The corresponding phase space distribution is shown in Fig. 6(e). With the transport of beam electrons in the first quartz tube, the beam size gradually increases with the form of $r_1(z)$ shown in Fig. 5(a) under the action of the defocusing magnetic field, and the phase space locates in the

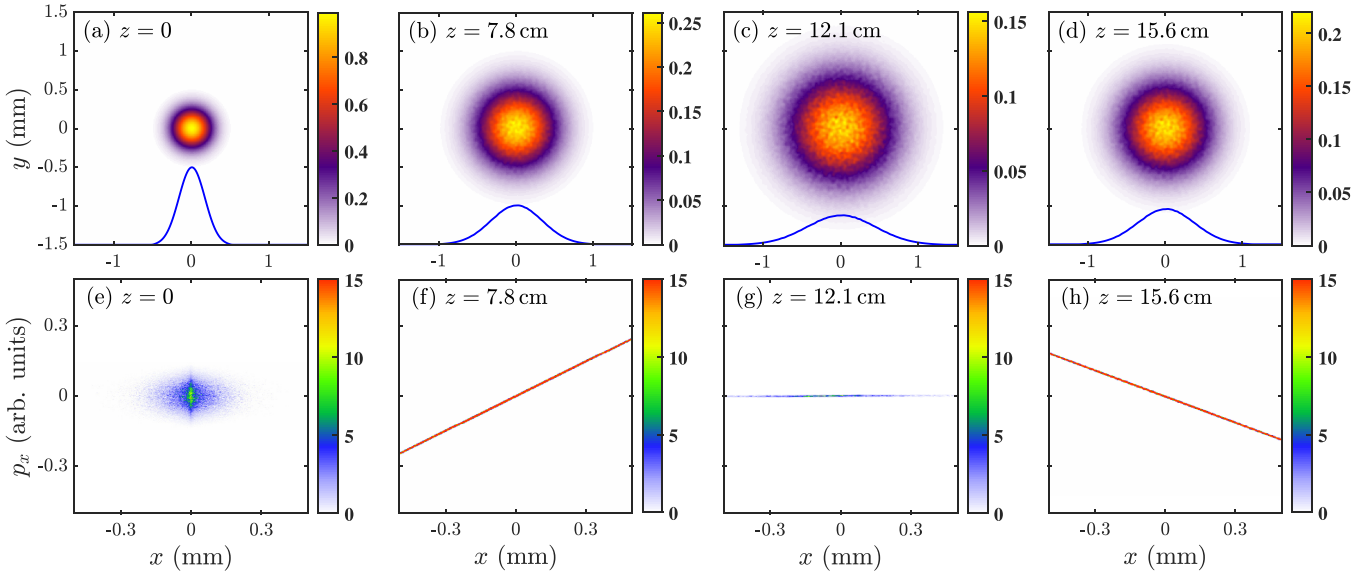

FIG. 6. PIC simulation results of the electron beam density n_{be} (a)–(d) and the transverse phase-space x-p_x distributions (e)–(h) for the plasma target with discharge current 1.5 kA. (a) and (e), (b) and (f), (c) and (g), and (d) and (h) correspond to the beam propagation distances of 0, 7.8 cm, 12.1 cm, and 15.6 cm, respectively. The insets in (a)–(d) display the corresponding beam slice profiles.

first and third quadrants, as indicated in Figs. 6(b) and 6(f). At $z = 12.1$ cm [Figs. 6(c) and 6(g)], the beam size reaches the maximum, as indicated by the phase space distribution. Finally, at the exit of the plasma target [Figs. 6(d) and 6(h)], the beam spot size is slightly reduced, but still larger than the initial one, and the phase space has a significant rotation and distributes in the second and fourth quadrants. The beam slice profiles at the four travel distances are also shown in Figs. 6(a)–6(d). They fit well with the analytical results in Fig. 5(a): $r/r_0 \sim 2$ at $z = z_1 = 7.8$ cm, $r/r_0 \sim 2.7$ at $z = z_2 = 12.1$ cm, and $r/r_0 \sim 2.3$ at $z = 15.6$ cm. At the exit of the plasma target, the electron beam is in the focusing phase, thus we can observe the focusing effect on the YAG screen.

Parameter scans are performed with different beam energies ε_{be} [30 MeV and 50 MeV] and discharge currents from 0 to 1.5 kA to show in detail the effects of plasma currents on beam focusing. Simulated beam spots at the same longitudinal position as that of the YAG screen in the experiment (i.e., 25.5 cm downstream the plasma target) are shown in Figs. 7(b)–7(d) and 7(f)–7(h). In the case of 50 MeV, the maximum beam focusing occurs at $I_{pe} = 0.7$ kA [Fig. 7(b)], and the beam density compared with Fig. 7(a) (discharge off) is increased by a factor of ~10, and the beam spot size is reduced by a factor of ~3 [see Fig. 7(b)]. The simulation results are in qualitative agreement with the experimental results. With the increase of the discharge current, the focal length becomes shorter, and the overfocusing effect can be observed in Figs. 7(c) and 7(d).

We also show here the electron beam with a lower energy of 30 MeV, and the beam density profiles are shown in Figs. 7(e)–7(h). A lower beam energy, thus a smaller Lorentz factor, leads to a shorter focal length. Therefore, a more significant overfocusing effect can be observed with the discharge current 1.5 kA [comparing Figs. 7(d) and 7(h)], which shows good agreement with the experimental results shown in Fig. 2(b). It should be noted here that due to a stronger overfocusing in the case of 30 MeV–1.5 kA, a larger simulation region is used in Fig. 7(h). The overfocusing effect can also be expected from Fig. 5(b). At the exit of the plasma target, the beam spot sizes in the cases of 30 MeV–1.5 kA (blue solid line) and 50 MeV–1.5 kA (red solid line) are almost the same. However, the beam electrons with energy 30 MeV have a higher radial velocity and thus, a shorter focal length. The maximum beam focusing at the screen for the two energy cases are compared in Figs. 7(b) and 7(f). The required plasma currents for maximum focusing are shown to increase with beam energy (i.e., 0.4 kA for 30 MeV. and 0.7 kA for 50 MeV), showing qualitative agreement with the experimental results in Fig. 2(b).

It should be noted here that the beam spot size in the experiment is much larger than that in the simulation. In addition, the plasma currents required for maximum beam focusing in simulations are lower than that in experiments. The underlying physics is relevant to the titanium films located on both sides of the plasma target. Note that an electron beam undergoes multiple scattering effects when passing through a material with finite thickness. The strong scattering in the titanium films significantly increases the beam emittance thus the spot size, which can be calculated statistically. The deflection angle produced by the multiple Coulomb scattering is approximately Gaussian shaped for a small angle. Supposing this small angle limit and considering that a parallel beam enters the titanium film, the rms angle of the beam electrons emerging from the film, $\sigma_{\theta,\,\mathrm{film}}$, is given by [33]

$$\sigma_{\theta,\,\mathrm{film}} = \frac{13.6\,\mathrm{MeV}}{\beta c p} Z \sqrt{\frac{x_0}{X_0}} \left[1 + 0.038 \ln\left(\frac{x_0}{X_0}\right)\right], \qquad (4)$$

where p is the beam momentum, βc is the beam velocity, Z is the charge number of the beam ($Z = 1$ for electron), x_0 is the thickness of the film (20 μm in this experiment), and X_0 is the radiation length of the material. The radiation length of tita-

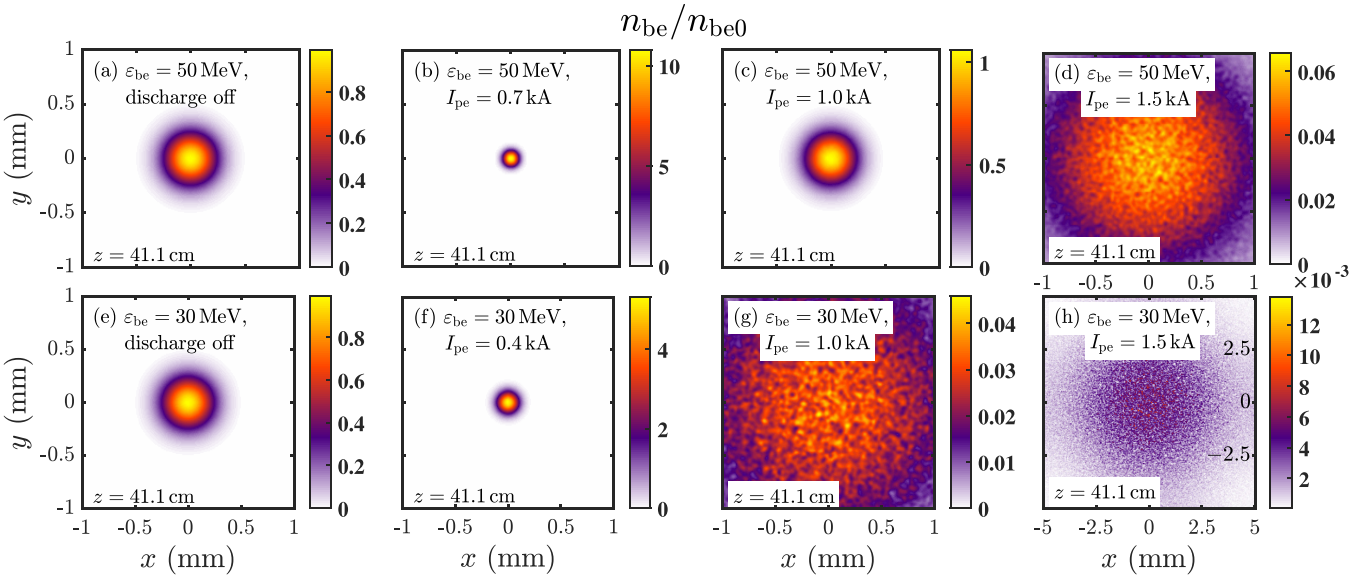

FIG. 7. Simulated beam spots at the same longitudinal position as that of the YAG screen in the experiment (i.e., 25.5 cm downstream the plasma target) for two beam energy cases: 50 MeV (b)–(d) and 30 MeV (f)–(h). (a) and (e): for reference, i.e., the beam spot at the screen with plasma discharge turned off. (b) and (f) represent the maximum beam focusing at the screen for the two energy cases, with the required plasma currents displayed in the figure. (c) and (g) and (d) and (h) refer to the cases of plasma currents 1 kA and 1.5 kA, respectively. Also, because of a stronger overfocusing in the case of 30 MeV–1.5 kA, a larger simulation region is used in (h).

nium [34] is 16.16 g · cm^{-2}. From Eq. (4) the angular spread that an electron beam with $\varepsilon_{be} = 50$ MeV gains by passing through two 10 μm titanium films is $\sigma_{\theta,\,\mathrm{film}} = 4.6$ mrad. With this scattering angle, the beam spot size increases by 1.17 mm [$\approx$25.5 cm $\times$ tan(4.6 mrad)] after a vacuum drift section of 25.5 cm. With an initial value of 0.167 mm, the beam size at the screen should be 1.3 mm, consistent with the experimental result (i.e., 1.25 mm) in Fig. 3(a) for the case of plasma discharge off. The beam emittance increases due to the scattering in titanium films, and a higher plasma current required for the maximum beam focusing can thus be expected in the experiment.

V. CONCLUSION

In conclusion, a plasma lens experiment was performed at IMP by employing a gas-discharge plasma target and accelerator electron beams, which is the first step toward the experimental validation of potential application of plasma lens in high-quality gamma-ray generation. The plasma with density $\sim 10^{23}$ m^{-3} is generated by igniting an electric discharge in two collinear quartz tubes, with the currents up to 1.5 kA flowing in opposite directions in either of the two tubes. In such a plasma current configuration, the electron beam is defocused in the first discharge tube and focused with a stronger force in the second one, leading to a factor of 2.6 reduction in beam radius compared to the case of plasma discharge off. The experimental results are supported by 2D PIC simulations and also an analysis of beam electron trajectory in the radial direction.

In this work, a low-charge accelerator electron beam with a beam density much smaller than plasma density is adopted for study. In future experiments, the accelerator electron beams with higher charge will be considered, in which case the beam self-focusing effects due to the unneutralized beam current in plasmas becomes important. In addition, with the increase of beam density, beam-plasma instabilities [35–38] may show important influences on beam transport. For the electron beams with finite sizes in the laboratory, the competition between the beam self-focusing and the instability excitation is a key issue [29,39]. In the next step, the plasma lens focused electrons beam will be sent through a conversion target for gamma-ray generation and the properties of the generated gamma-ray will be compared for the cases of plasma lens on and off.

ACKNOWLEDGMENTS

This work is supported by the National Natural Science Foundation of China (Project No. 12075046).

[1] W. P. Leemans, C. G. R. Geddes, J. Faure, C. Tóth, J. van Tilborg, C. B. Schroeder, E. Esarey, G. Fubiani, D. Auerbach, B. Marcelis, M. A. Carnahan, R. A. Kaindl, J. Byrd, and M. C. Martin, Phys. Rev. Lett. **91**, 074802 (2003).

[2] W. Leemans, E. Esarey, J. van Tilborg, P. Michel, C. Schroeder, C. Toth, C. Geddes, and B. Shadwick, IEEE Trans. Plasma Sci. **33**, 8 (2005).

[3] C. B. Schroeder, E. Esarey, J. van Tilborg, and W. P. Leemans, Phys. Rev. E **69**, 016501 (2004).

[4] Z.-H. Hu, X.-J. Wang, D.-X. Hui, Q.-T. Zhao, R. Cheng, Y.-T. Zhao, Z.-M. Zhang, and Y.-N. Wang, Phys. Plasmas **27**, 023103 (2020).

[5] Y. Glinec, J. Faure, L. L. Dain, S. Darbon, T. Hosokai, J. J. Santos, E. Lefebvre, J. P. Rousseau, F. Burgy,

B. Mercier, and V. Malka, Phys. Rev. Lett. **94**, 025003 (2005).
[6] V. Senthilkumaran, D. Bailie, K. Behm, J. Warwick, G. M. Samarin, A. Maksimchuk, J. Nees, A. G. R. Thomas, G. Sarri, K. Krushelnick, and A. E. Hussein, Appl. Phys. Lett. **120**, 264103 (2022).
[7] J. J. Su, T. Katsouleas, J. M. Dawson, and R. Fedele, Phys. Rev. A **41**, 3321 (1990).
[8] T. Tajima and J. M. Dawson, Phys. Rev. Lett. **43**, 267 (1979).
[9] I. Dornmair, K. Floettmann, and A. R. Maier, Phys. Rev. ST Accel. Beams **18**, 041302 (2015).
[10] C. Patrignani, Chinese Phys. C **40**, 100001 (2016).
[11] I. Hofmann, Phys. Rev. ST Accel. Beams **16**, 041302 (2013).
[12] J. van Tilborg, S. Steinke, C. G. R. Geddes, N. H. Matlis, B. H. Shaw, A. J. Gonsalves, J. V. Huijts, K. Nakamura, J. Daniels, C. B. Schroeder, C. Benedetti, E. Esarey, S. S. Bulanov, N. A. Bobrova, P. V. Sasorov, and W. P. Leemans, Phys. Rev. Lett. **115**, 184802 (2015).
[13] A. W. Chao, K. H. Mess, M. Tigner, and F. Zimmermann, *Handbook of Accelerator Physics and Engineering*, 2nd ed. (World Scientific, Singapore, 2013).
[14] R. Pompili, M. P. Anania, M. Bellaveglia, A. Biagioni, S. Bini, F. Bisesto, E. Brentegani, F. Cardelli, G. Castorina, E. Chiadroni, A. Cianchi, O. Coiro, G. Costa, M. Croia, D. Di Giovenale, M. Ferrario, F. Filippi, A. Giribono, V. Lollo, A. Marocchino *et al.*, Phys. Rev. Lett. **121**, 174801 (2018).
[15] C. A. Lindstrøm, E. Adli, G. Boyle, R. Corsini, A. E. Dyson, W. Farabolini, S. M. Hooker, M. Meisel, J. Osterhoff, J.-H. Röckemann, L. Schaper, and K. N. Sjobak, Phys. Rev. Lett. **121**, 194801 (2018).
[16] J.-H. Röckemann, L. Schaper, S. K. Barber, N. A. Bobrova, G. Boyle, S. Bulanov, N. Delbos, K. Floettmann, G. Kube, W. Lauth, W. P. Leemans, V. Libov, A. R. Maier, M. Meisel, P. Messner, P. V. Sasorov, C. B. Schroeder, J. van Tilborg, S. Wesch, and J. Osterhoff, Phys. Rev. Accel. Beams **21**, 122801 (2018).
[17] R. Pompili, M. P. Anania, M. Bellaveglia, A. Biagioni, S. Bini, F. Bisesto, E. Brentegani, G. Castorina, E. Chiadroni, A. Cianchi, M. Croia, D. Di Giovenale, M. Ferrario, F. Filippi, A. Giribono, V. Lollo, A. Marocchino, M. Marongiu, A. Mostacci, G. Di Pirro *et al.*, Appl. Phys. Lett. **110**, 104101 (2017).
[18] A. Marocchino, M. P. Anania, M. Bellaveglia, A. Biagioni, S. Bini, F. Bisesto, E. Brentegani, E. Chiadroni, A. Cianchi, M. Croia, D. Di Giovenale, M. Ferrario, F. Filippi, A. Giribono, V. Lollo, M. Marongiu, A. Mostacci, G. Di Pirro, R. Pompili, S. Romeo *et al.*, Appl. Phys. Lett. **111**, 184101 (2017).
[19] C. E. Doss, E. Adli, R. Ariniello, J. Cary, S. Corde, B. Hidding, M. J. Hogan, K. Hunt-Stone, C. Joshi, K. A. Marsh, J. B. Rosenzweig, N. Vafaei-Najafabadi, V. Yakimenko, and M. Litos, Phys. Rev. Accel. Beams **22**, 111001 (2019).
[20] P. Chen, K. Oide, A. M. Sessler, and S. S. Yu, Phys. Rev. Lett. **64**, 1231 (1990).
[21] K. N. Sjobak, E. Adli, R. Corsini, W. Farabolini, G. Boyle, C. A. Lindstrøm, M. Meisel, J. Osterhoff, J.-H. Röckemann, L. Schaper, and A. E. Dyson, Phys. Rev. Accel. Beams **24**, 121306 (2021).
[22] C. Thaury, E. Guillaume, A. Döpp, R. Lehe, A. Lifschitz, K. Ta Phuoc, J. Gautier, J.-P. Goddet, A. Tafzi, A. Flacco, F. Tissandier, S. Sebban, A. Rousse, and V. Malka, Nat. Commun. **6**, 6860 (2015).
[23] A. P. Kuznetsov, O. A. Byalkovskii, R. O. Gavrilin, A. A. Golubev, K. L. Gubskii, I. V. Rudskoi, S. M. Savin, V. I. Turtikov, and A. V. Khudomyasov, Plasma Phys. Rep. **39**, 248 (2013).
[24] Q. Zhao, S. Cao, M. Liu, X. Sheng, Y. Wang, Y. Zong, X. Zhang, Y. Jing, R. Cheng, Y. Zhao, Z. Zhang, Y. Du, and W. Gai, Nucl. Instrum. Methods Phys. Res., Sect. A **832**, 144 (2016).
[25] Y. Zhu, P. Yuan, S. Cao, M. Liu, Y. Zong, Q. Zhao, J. Zhang, X. Shen, and Z. Zhang, Nucl. Instrum. Methods Phys. Res., Sect. A **911**, 74 (2018).
[26] G. Belyaev, M. Basko, A. Cherkasov, A. Golubev, A. Fertman, I. Roudskoy, S. Savin, B. Sharkov, V. Turtikov, A. Arzumanov, A. Borisenko, I. Gorlachev, S. Lysukhin, D. H. H. Hoffmann, and A. Tauschwitz, Phys. Rev. E **53**, 2701 (1996).
[27] Y. T. Zhao, Y. N. Zhang, R. Cheng, B. He, C. L. Liu, X. M. Zhou, Y. Lei, Y. Y. Wang, J. R. Ren, X. Wang, Y. H. Chen, G. Q. Xiao, S. M. Savin, R. Gavrilin, A. A. Golubev, and D. H. H. Hoffmann, Phys. Rev. Lett. **126**, 115001 (2021).
[28] S. Zhang, C. Chen, T. Lan, W. Ding, G. Zhuang, W. Mao, S. Lan, J. Wu, H. Xu, T. Deng, J. Zhu, J. Wu, Y. Zu, D. Kong, S. Zhang, Y. Yao, Z. Wei, Z. Liu, H. Zhou, H. Wang *et al.*, Rev. Sci. Instrum. **91**, 063501 (2020).
[29] H.-L. Li, Z.-H. Hu, Q.-T. Zhao, R. Cheng, Y.-T. Zhao, Z.-M. Zhang, X.-C. Li, and Y.-N. Wang, Phys. Plasmas **29**, 052101 (2022).
[30] B. Schmidt, N. M. Lockmann, P. Schmüser, and S. Wesch, Phys. Rev. Accel. Beams **23**, 062801 (2020).
[31] Z.-H. Hu and Y.-N. Wang, Phys. Plasmas **23**, 023103 (2016).
[32] X.-J. Wang, Z.-H. Hu, Y.-T. Zhao, and Y.-N. Wang, Phys. Plasmas **25**, 102104 (2018).
[33] M. C. Thompson, H. Badakov, J. B. Rosenzweig, G. Travish, N. Barov, P. Piot, R. Fliller, G. M. Kazakevich, J. Santucci, J. Li, and R. Tikhoplav, Phys. Plasmas **17**, 073105 (2010).
[34] K. Hagiwara, K. Hikasa, K. Nakamura, M. Tanabashi, M. Aguilar-Benitez, C. Amsler, R. M. Barnett, P. R. Burchat, C. D. Carone, C. Caso, G. Conforto, O. Dahl, M. Doser, S. Eidelman, J. L. Feng, L. Gibbons, M. Goodman, C. Grab, D. E. Groom, A. Gurtu *et al.* (Particle Data Group), Phys. Rev. D **66**, 010001 (2002).
[35] A. R. Bell and R. J. Kingham, Phys. Rev. Lett. **91**, 035003 (2003).
[36] J. R. Davies, A. R. Bell, and M. Tatarakis, Phys. Rev. E **59**, 6032 (1999).
[37] F. Califano, R. Prandi, F. Pegoraro, and S. V. Bulanov, Phys. Rev. E **58**, 7837 (1998).
[38] F. Califano, N. Attico, F. Pegoraro, G. Bertin, and S. V. Bulanov, Phys. Rev. Lett. **86**, 5293 (2001).
[39] P. San Miguel Claveria, X. Davoine, J. R. Peterson, M. Gilljohann, I. Andriyash, R. Ariniello, C. Clarke, H. Ekerfelt, C. Emma, J. Faure, S. Gessner, M. J. Hogan, C. Joshi, C. H. Keitel, A. Knetsch, O. Kononenko, M. Litos, Y. Mankovska, K. Marsh, A. Matheron *et al.*, Phys. Rev. Res. **4**, 023085 (2022).